

Quantifying the Morphology and Mechanisms of Cancer Progression in 3D *in-vitro* environments: Integrating Experiments, Multiscale Models, and Spatial Validation

Nikolaos M. Dimitriou, Salvador Flores-Torres, Joseph Matthew Kinsella, and Georgios D. Mitsis

Abstract—Throughout the years, mathematical models of cancer growth have become increasingly more accurate in terms of the description of cancer growth in both space and time. However, the limited amount of data typically available has resulted in a larger number of qualitative rather than quantitative studies. In this study, we provide an integrated experimental-computational framework for the quantification of the morphological characteristics and the mechanistic modelling of cancer progression in 3D environments. The proposed framework allows for the calibration of multiscale-spatiotemporal models of cancer growth using 3D cell culture data, and their validation based on the morphological patterns. The implementation of this framework enables us to pursue two goals; first, the quantitative description of the morphology of cancer progression in 3D cultures, and second, the relation of tumour morphology with underlying biophysical mechanisms that govern cancer growth. We apply this framework to the study of the spatiotemporal progression of Triple Negative Breast Cancer (TNBC) cells cultured in 3D Matrigel scaffolds, under the hypothesis of chemotactic migration using a multiscale Keller-Segel model. The results reveal transient, non-random spatial distributions of cancer cells that consist of clustered patterns across a wide range of neighbourhood distances, as well as dispersion for larger distances. Overall, the proposed model was able to describe the general characteristics of the experimental observations and suggests that cancer cells exhibited chemotactic migration and cell accumulation, as well as random motion throughout the period of development. To our knowledge, this is the first time a framework attempts to quantify the relationship between the spatial patterns and the underlying mechanisms of cancer growth in 3D environments.

Index Terms—3D cell cultures, confocal microscopy, multiscale models, spatiotemporal model validation

I. INTRODUCTION

This work was enabled in part by support provided by Cyprus Research and Innovation Foundation (Project: INTERNATIONAL/OTHER/0118/0018) and Compute Canada (www.computeCanada.ca). (Corresponding author: Nikolaos M. Dimitriou)

The authors are with the Department of Bioengineering, McGill University, Montreal, QC, H3A 0E9, Canada (email: nikolaos.dimitriou@mail.mcgill.ca; salvador.florestorres@mail.mcgill.ca; joseph.kinsella@mcgill.ca; georgios.mitsis@mcgill.ca)

This article has supplementary downloadable material available at <https://ieeexplore.ieee.org>, provided by the authors.

CANCER progression is frequently accompanied by migration of cancer cells into the surrounding tissues, that eventually leads to metastasis. Both *in-vivo* and *in-vitro* studies of cancer cell migration have shown that cancers can exhibit several types of patterns including single cell migration, multicellular streaming, collective cell migration, as well as passive patterns, such as tissue folding, and expansive growth [1]. Studies of breast cancer have shown that the tumour border is dominated by collective cell migration [1] forming small acinar structures with a central luminal space, with cancer cells that maintain their epithelial morphology [2]. Evidence of multicellular streaming also exist from orthotopic breast cancer in xenograft mouse models [3]. Other clinical studies of the surface morphology of infiltrating ductal adenocarcinoma have shown that the fractal dimension of cancerous tissue is larger compared to normal breast tissue [4]. Similar observations of different fractality characteristics in different tumour stages have also been made in ovarian cancer [5]. Though there is significant knowledge on the qualitative aspects of tumour morphology, the quantitative characterization of this morphology and the biophysical mechanisms that govern cancer growth remain still elusive.

Significant insights into both morphological and mechanistic characteristics of cancer growth can be gained from the use of mathematical models. The spatiotemporal models of cancer growth can be distinguished in three general categories; discrete (e.g. agent based models), continuum (Partial Differential Equations, PDEs), and hybrid models [6]. Each of these categories provides different information on the aspects of tumour growth. Specifically, discrete models can provide information on individual cell processes or tissue microarchitecture [7]. Continuum models have been widely used, initially to describe qualitative aspects of tumour growth, despite lacking experimental validation [8], and more recently, for a more detailed quantitative description of the macroscopic characteristics of spatiotemporal cancer growth and its response to therapy in both *in-vitro* [9]–[12] and *in-vivo* conditions [13]–[19]. Hybrid models attempt a multiscale description of cancer growth, by incorporating both continuous and discrete variables [20], [21]. Studies from Tweedy et al. [22], [23] utilized experiments and hybrid discrete-continuum (HDC) models of chemotactic migration to investigate the role

of self-generated chemotactic gradients in cancer migration. Even though there is an expanding literature on spatiotemporal models of cancer, their validation using experimental data is important for quantitatively describing cancer [24], [25].

The validation of a model can be interpreted as the process of determining the accuracy of a model representation of a real tumour [24]. Validation usually comes after the calibration of the model, which is usually defined as the process of inferring the model parameters that provide the best fit between model predictions and experimental data. In the work of Hawkins-Daarud et al. [26] a Bayesian framework was used for the validation of diffuse-interface models of tumour growth using synthetic data. Achilleos et al. [27], [28] utilized stochastic processes for the validation of a mixture-model using tumour measurements obtained from experiments in mice. Lima et al. [25] employed the Occam Plausibility Algorithm (OPAL) [29] to validate various classes of PDE models using images of glioma tumours in mice. Recently, they [30] studied the calibration of hybrid models with *in-vitro* 2D culture data. Although, these studies provide a significant advances in model validation, the application of this knowledge in tumour modelling is still lacking.

A common reason for the absence of validation in tumour modelling studies is the lack of data availability. *In-vitro* studies usually include the use of 2D cultures [11], [12], resulting in a less realistic representation of cancer growth. *In-vivo* studies, both clinical and experimental, can be more realistic; however, they also present limitations. On the one hand, caliper and microCT scan measurements of *in-vivo* tumours in mice do not typically provide information on tumour shape and invasiveness [31], [32]. Intravital imaging is another common way of data collection for *in-vivo* models; however, this technique suffers from technical challenges such as passive drift of cells or tissues, low penetration depth, tissue heating, and limitations on imaging intervals [1]. On the other hand, data from clinical cases can be limited [15], resulting in model over-fit.

To this end, 3D cell culture models have become a promising experimental tool. The main reasons are the increased control of the experimental conditions, the flexibility of data collection compared to *in-vivo* experiments, and their more realistic representation of tumour progression compared to 2D cultures. Differences between 3D and 2D cultures have been observed in cancer growth and its related biochemical processes, such as the secretion of extracellular matrix (ECM) components, and cell-cell interaction components [33], while the histological and molecular features of *in-vitro* 3D spheroids exhibit more similarities with xenografts than 2D monolayers [33]. Significant differences between 2D and 3D cultures have also been found in drug testing studies exhibiting alterations in the sensitivity of cytotoxic drugs [33]. Another advantage of 3D cell culture models is their flexibility with regards to incorporating more than one cell populations, such as stromal cells, as well as on changing the stiffness of the ECM. The heterotypic intercellular interactions between cancer cells and stromal cells results in altered cancer cell proliferation and migration, as well as the formation of more compact spheroids compared to equivalent 3D cell mono-culture systems [33].

The mechanical properties of the ECM also contribute to the spheroid formation, viability, invasiveness, and drug sensitivity of cancer cells [33]. Additionally, the collection of imaging data for *in-vitro* 3D cell cultures is generally easier and more accurate than *in-vivo* models, and high resolution images can be obtained using confocal microscopy. Although 3D cell cultures cannot yet capture the full complexity of tumour growth in a living tissue, overall they yield significant potential for quantitatively describing cancer growth, as they even provide the opportunity to track even single cells.

The purpose of the present work is to introduce a framework for the quantitative characterization of spatiotemporal progression of cancer, and its use in multiscale-spatiotemporal model validation for the study of mechanisms of cancer growth. The framework presented in Fig. 1 proposes a novel combination of experimental data from 3D cell cultures, spatial statistical analysis techniques for the quantification of cancer morphology, and a multiscale HDC mathematical model for the quantitative description of the mechanisms underlying cancer progression. Given the spatial scales (μm up to mm) of the 3D cultures, the choice of HDC models instead of purely continuum or discrete models is based on the fact that HDC models allow us to perform faster calibration on the continuum model component, albeit with a lower fidelity compared to the full model, and validation on the discrete component, hence achieving richer evaluations and statistical comparisons for its validity. The introduction of the spatial pattern analysis not only helps by improving the validation of hybrid models, but also interpreting the observed patterns based on the underlying mechanisms. The rest of the article is organized in a Methods section, where we describe the experiments, data processing, the mathematical model, the calibration and validation techniques, followed by the Results where we present the calibrated model, the validity tests of the full model, as well as a discussion on the relation between morphology and the underlying mechanisms. Finally, we conclude with the Discussion and Conclusions, where we discuss our results compared to relevant literature, the advantages and limitations of this study, as well as possible extensions and improvements. The code and data of this work are available at <https://nmdimitriou.github.io/HyMetaGrowth/>.

II. METHODS

A. Experiments

Cell preparation: Triple Negative Breast Cancer (TNBC) cells from the MDA-MB-231 cell line with nuclear GFP (histone transfection), were thawed and cultured at 5% CO₂, 37 °C in DMEM (Gibco) at pH 7.2 supplemented with 10% fetal bovine serum (Wisent Bioproducts), 100 U/mL penicillin, 100 $\mu\text{g}/\text{mL}$ streptomycin, and 0.25 $\mu\text{g}/\text{mL}$, and amphotericin B (Sigma) in T-75 flasks (Corning). The cells were passaged before reaching 85% confluence. Three passages were performed before the 3D cultures; cells were rinsed twice with DPBS and trypsin-EDTA (0.25%-1X, Gibco) was used to harvest them.

3D cell cultures: A cell-Matrigel (Corning) suspension was created using 0.25 mL of Matrigel (4 °C) and 5×10^4 MDA-MB-231/GFP cells. Droplets of 5 μL cell-Matrigel mixture

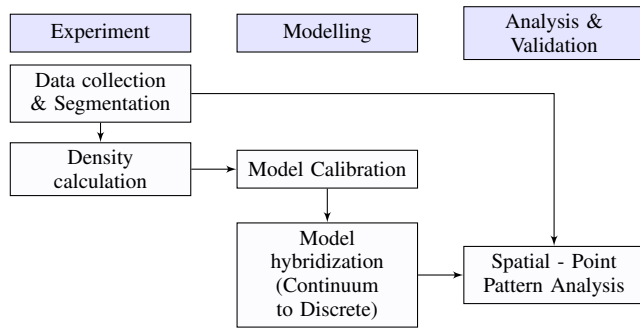


Fig. 1: Proposed pipeline for the modelling, validation and analysis of cancer progression using *in-vitro* 3D experimental data.

were manually deposited onto a high performance #1.5 glass bottom 6-well plate (0.170 ± 0.005 mm) (Fisher Scientific) (Fig. 2a). In total, 12 datasets were produced with 7 samples on days 0, 2, 5, 7, 9, 12, 14 each. (Fig. 2b-2f).

Imaging and Data preparation: Data acquisition was performed every 2-3 days for a total of 15 days using a confocal microscope (Nikon A1R HD25) coupled with a cell-culture chamber. The dimensions of the 3D cultures were approximately $2.5 \times 2.5 \times 0.9$ mm³. Cell localization was made possible by the GFP fluorophore that was present in cell nuclei. The fluorescent nuclei were segmented using an image processing and segmentation pipeline consisting of two parts; an image preprocessing and a segmentation part [34]. The preprocessing of the image stacks includes: (i) image denoising using the Poisson Unbiased Risk Estimation-Linear Expansion of Thresholds (PURE-LET) technique [35], (ii) intensity attenuation correction across the z -dimension [36], (iii) background subtraction using the rolling ball algorithm [37] and manual thresholding of low intensity values using High-Low Look Up Tables (HiLo LUTS), and (iv) cubic spline interpolation of the xy -planes of the image stacks. The segmentation of the nuclei was performed using Marker Controlled Watershed segmentation and a classic Distance Based Watershed segmentation to split fused nuclei (Fig. 2g-2k). The segmented nuclei were then mapped to a 3D Cartesian space by detecting their centroids using a 26-connected neighbourhood tracing algorithm implemented in MATLAB [38]. The final step was the calculation of spatial density profiles of the cells represented by their centroids, using the Kernel Density estimation via the Diffusion method found in [39]. The density calculation was in a grid of size $167 \times 167 \times 61$ such that each cell approximately occupies one grid point. The density matrices were interpolated, using linear interpolation, to match the spatial grid size of the simulations ($480 \times 480 \times 176$).

B. Multiscale HDC Model

Chemotactic hypothesis: Previous studies [40] have shown that cells in 3D cultures using hydrogel matrices such as Collagen I or Matrigel tend to move towards the bottom of the space. We hypothesized that this behaviour occurs due to three main reasons; first, the MDA-MB-231 cells are naturally

adherent cells, hence the cells need to remain attached to each other to function properly; second, at the beginning and throughout the course of the experiment, the cells secrete chemotactic signals that enable cell migration and tend to bring the cells closer to each other; third, the cells that are closer to the glass bottom secrete signals at the beginning of the experiment creating a chemotactic gradient decreasing from the bottom towards the top of the space. The reason behind the third hypothesis is that the glass is a surface that favours cell attachment, hence the cells that are closer to this surface secrete these signals to indicate it as a site of preference. This hypothesis is supported by recent findings on self-generated chemotactic gradients [22], [23], [41], [42] with the difference that we assumed that the chemoattractants stem from the cells and they do not pre-exist in the 3D space.

Continuum model: To examine this hypothesis, we used a system of two Keller-Segel (KS) type equations for cancer cell density and chemotactic agent density that additionally takes into account random motion of cancer cells and chemotactic agents, logistic growth of cancer cells, and increase of chemotactic agents depending on their current concentration in the space and the presence of cancer cells. The spatiotemporal evolution of cancer cell, u , and chemotactic agent, f , densities are defined in the following PDEs:

$$\frac{\partial u}{\partial t} = D_u \nabla^2 u + su(1-u) - \chi \nabla \cdot [u(1-u) \nabla f], \quad \text{in } \Omega \quad (1)$$

$$\frac{\partial f}{\partial t} = D_f \nabla^2 f + \rho f u(1-u), \quad \text{in } \Omega \quad (2)$$

$$\nabla u \cdot \vec{n} = \nabla f \cdot \vec{n} = 0, \quad \text{in } \partial \Omega \quad (3)$$

where D_u , D_f are the diffusion constants, and s , ρ are the growth constants of the cell and signal densities, respectively, and χ is the advection constant of the cell density. The right hand side of (1) consists of three terms; the diffusion term $D_u \nabla^2 u$ that represents the random motion and expansive growth of the cancer cells, the growth term $su(1-u)$ that increases the density of the tumour in a logistic manner, and the nonlinear advection term $-\chi \nabla \cdot [u(1-u) \nabla f]$ that represents the biased movement of the cell densities towards the direction where the gradient of the chemotactic signal density increases. The $(1-u)$ factor in the advection term was added to avoid unwanted overcrowding of the cells that can lead to spikes of cell density [43]. In (2) the evolution of the signal density depends on the diffusion of the signal in 3D space, represented by $D_f \nabla^2 f$ and the production of signals depending on the current signal density and cell density in space, $\rho f u(1-u)$. Similarly, $(1-u)$ limits the signal when overcrowding takes place. The spatial domain Ω has the same size as the domain of the experimental data, $2.5 \times 2.5 \times 0.917$ mm³, and it is represented by $480 \times 480 \times 176$ grid points. We consider no-flux Neumann boundary conditions (B.C.) in (3), where \vec{n} is the outward unit normal to $\partial \Omega$.

The initial conditions (I.C.) for this problem were chosen based on the experimental data and the chemotactic hypoth-

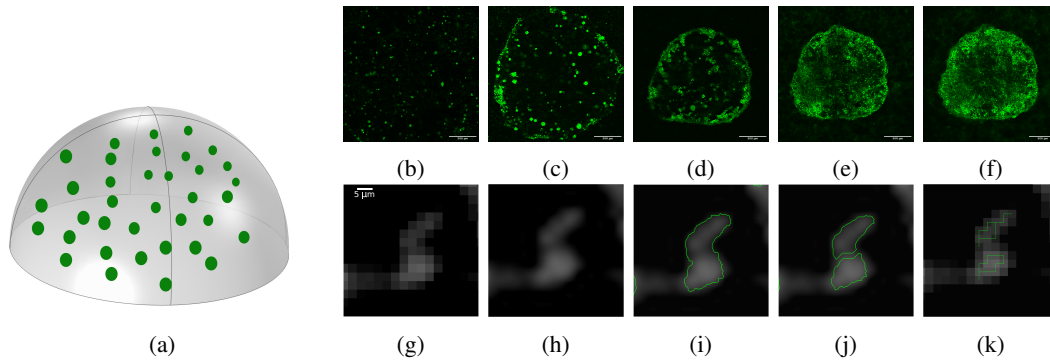


Fig. 2: 3D cell cultures and nucleic segmentation. (a) Schematic representation of the cell/Matrigel geometry at Day 0 of the experiment. Slices at $Z \approx 100 \mu\text{m}$ from the bottom of the plate on days (b) 5, (c) 7, (d) 9, (e) 12, (f) 14. Scale bar: $500 \mu\text{m}$. (g) Zoomed image of two cells on day 9. (h) Interpolation result resulting from (h). (i) Marker Controlled Watershed segmentation. (j) Nuclei splitting with Distance Based Watershed segmentation. (k) Rescaling back to original image size.

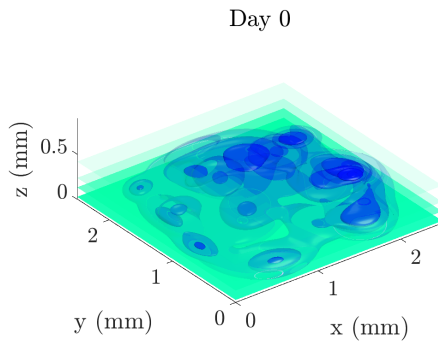


Fig. 3: Initial conditions of the continuum model from one of the 12 datasets. The blue colour map represents the cell density profile, u , and it is directly obtained from the experimental data. The green colour map represents the chemotactic agents density profile, f and it is calculated using (4).

esis. Specifically, the initial cell density profiles of the simulations were chosen to be the spatial cell density profiles of Day 0 of the experiment. The I.C. for the chemotactic signals were based on the fact that the cells are, initially, uniformly distributed in the 3D space, and they separate from each other. Cells attached to the bottom glass secrete chemotactic agents first, which in turn promotes the secretion of these agents by the above floating cells as described in (4).

$$f(x, y, z, t = 0) = e^{-\frac{z}{0.26(\text{mm})}} I(u), \quad I(u) = \begin{cases} 1, & \text{if } u > 0 \\ 0, & \text{if } u = 0 \end{cases} \quad (4)$$

The I.C. of the model for one of the datasets are shown in Fig. 3.

Numerical methods: We used the operator-splitting technique to approximate the diffusion, advection, and reaction operators. The diffusion terms were approximated by the Alternating Direction Implicit (ADI) Douglas-Gunn (DG) method [44]. The advection term was approximated by the explicit Lax-Wendroff (LxW) method [45], coupled with the Monotonic Upstream-Centered Scheme for Conservation Laws (MUSCL) flux limiter [46]. The integration in time was

performed using the Strang splitting scheme [47]. At every time-step, the Strang splitting scheme evolves the advection and reaction terms for $0.5dt$, then the diffusion operator for dt , and then again the advection and reaction operators for $0.5dt$. The accuracy of this scheme is second-order for both space and time. The proposed numerical scheme was implemented on GPUs using the CUDA/C programming language. Each simulation required approximately 1-5 minutes to complete in a V100-16GB Nvidia GPU (Supplementary S1).

Hybrid model: We hybridized the KS model based on the technique presented in [48], [49]. We discretized (1) using the forward time central differences scheme (FTCS) using the approximations found in [50]:

$$u_{i,j,k}^{n+1} = u_{i,j,k}^n P_0 + u_{i+1,j,k}^n P_1 + u_{i-1,j,k}^n P_2 + u_{i,j+1,k}^n P_3 + u_{i,j-1,k}^n P_4 + u_{i,j,k+1}^n P_5 + u_{i,j,k-1}^n P_6 \quad (5)$$

where the grouped terms P_i , $i = 0, \dots, 6$ denote probabilities of the cells of remaining stationary (P_0) or moving back (P_1), front (P_2), left (P_3), right (P_4), down (P_5), up (P_6), defined as

$$P_0 = 1 - \frac{6D_u dt}{dx^2}$$

$$P_{1,2} = \frac{D_u dt}{dx^2} \mp \frac{\chi dt}{4dx^2} (f_{i+1,j,k} - f_{i-1,j,k})$$

$$P_{3,4} = \frac{D_u dt}{dx^2} \mp \frac{\chi dt}{4dx^2} (f_{i,j+1,k} - f_{i,j-1,k})$$

$$P_{5,6} = \frac{D_u dt}{dx^2} \mp \frac{\chi dt}{4dx^2} (f_{i,j,k+1} - f_{i,j,k-1}) \quad (6)$$

Since the cells were approximately $15 \mu\text{m}$ in size and the spatial grid points had a distance of $5.2 \mu\text{m}$ between each other, we assumed that each cell occupied 3 grid points in each direction. In turn, we modified the aforementioned scheme of (5), (6) by changing the indices that point to a direction to two grid points instead of one, i.e. $i \pm 1$ will be $i \pm 2$ etc. The moving probabilities were then passed to a cellular automaton that updated the position and state of each cell.

The cellular automaton (CA) is presented in Fig. 4a. The CA takes into account three cellular states; alive, quiescent and dead. At every time step it, checks if a cell can undergo spontaneous death based on the probabilities presented in

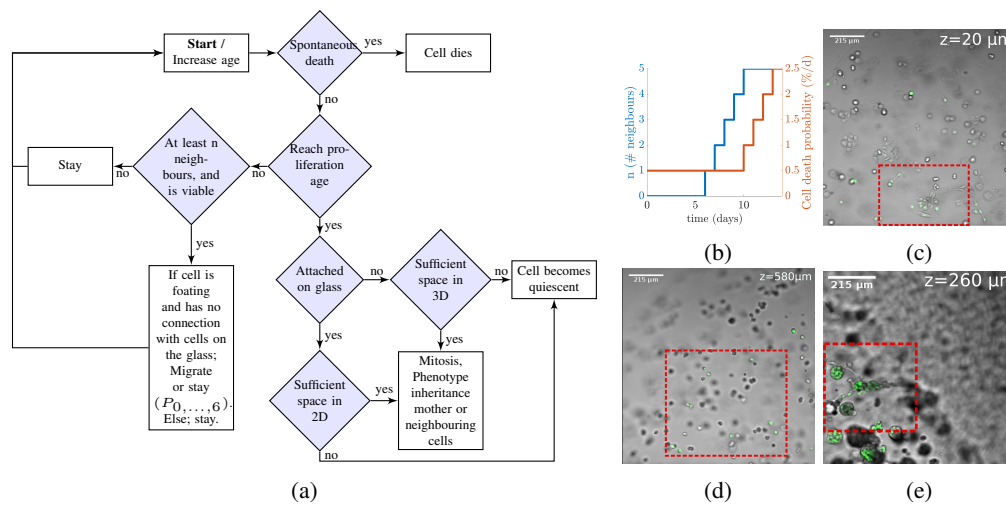


Fig. 4: (a) Flowchart of the cellular automaton used in this study. (b) Migration, adhesion, and cell death probability parameters of the cellular automaton were changed over time. (c) Cells settled at the bottom ($z=20 \mu\text{m}$), and (d) cells floating at $z=580 \mu\text{m}$ on Day 2. Cells settled on the bottom had stellar shapes, while cells floating in the Matrigel had rounder shapes. (e) Cells floating at $z=260 \mu\text{m}$ on Day 7. Some floating cells changed to stellar shapes resembling those attached on the bottom, as shown in panel (c).

Fig. 4b, and updates the age of the alive cells. The spontaneous death probability was increased after Day 10. This hypothesis was based on the increased cell crowding, which resulted in a potential shortage of nutrients or accumulation of metabolic waste products. The CA checks if any cell has reached the proliferation age that is determined based on the estimated parameter s (days)⁻¹ of the continuum model. We estimated the doubling time from the exponential phase of growth, e^{st} , and the resulting formula $t_{\text{double}} = \ln 2/s$. If a cell is ready to divide, the algorithm separates into two processes based on cell position in space. If the cell is attached on the glass and there is sufficient space, then the division will be performed on the glass; otherwise the cell will divide in any direction of the 3D space if there is sufficient space. On the other hand, if there is not sufficient space, the cell becomes quiescent. If the cell is not ready to divide, the CA turns to a migration program. The first condition for migration considers an adhesion parameter, defined as the number of neighbours that surround a cell, and the second is the state of the cell. We hypothesized that the number of neighbours required for cell migration increases over time (Fig. 4b), due to the fact that the initial distribution of cells in the 3D space is sparse; hence they migrate, freely, to search for other cells to attach, but as cell clustering occurs due to cell division or cell contact, migration becomes less frequent since the cells are attached to each other. If a cell satisfies these conditions, the algorithm checks the position of the cell. If a cell is settled on the bottom of the space or is connected with a cell located on the bottom, it cannot migrate; otherwise, the cell can migrate in 3D space given the moving probabilities P_0, \dots, P_6 . These two, constrained and unconstrained, migration phenotypes resemble epithelial and mesenchymal phenotypes, respectively, and the transition between them can be found in the literature as mesenchymal to epithelial transition (MET) [51]. Indeed, changes in cellular morphology were observed between cells settled on the bottom

and cells floating in Matrigel. In Fig. 4c, 4d we observe that floating cells during the early days of the experiment. However, at later time-points (Fig. 4e), we observed stellar shapes in floating cells probably, due to increased adhesion between them.

C. Bayesian Inference for calibration of the continuum model

The Keller-Segel model, M , (Eq (1)-(3)) has a set of parameters $\theta = \{D_u, s, \chi, D_f, r\}$ that are considered unknown. We used their Probability Distribution Functions (PDF) and the calculated densities from the 3D cell culture data, \mathcal{D} , to assess the most probable parameter values according to Bayes' rule

$$\mathbb{P}(\theta|\mathcal{D}, M) \propto \mathbb{P}(\mathcal{D}|\theta, M)\mathbb{P}(\theta) \quad (7)$$

where $\mathbb{P}(\theta|\mathcal{D}, M)$ is the posterior PDF of the model parameters θ given the observed data \mathcal{D} and the model M , $\mathbb{P}(\mathcal{D}|\theta, M)$ is the likelihood of the observed data \mathcal{D} given the model M and the parameters θ , and $\mathbb{P}(\theta)$ is the prior PDF. We assume uninformative, uniform distributions for the model parameter prior PDFs. The experimental data consisted of 12 datasets and each of them had samples from 7 time-points. The datasets were assumed to be independent and the model was evaluated for each dataset separately. The likelihood and log-likelihood were defined as

$$L(\theta; \mathbf{d}) = \prod_{i=1}^n \frac{1}{\sigma_d \sqrt{2\pi}} \exp\left(-\frac{(d_i - q_i(\theta))^2}{2\sigma_d^2}\right) \quad (8)$$

where n is the number of spatial grid points, \mathbf{d} the density profile of the corresponding sample in a dataset, d_i , q_i the density values of the experimental sample and simulation result, respectively, at the grid point i , and σ_d the variance of the distribution of the likelihood.

We used a Transitional Markov Chain Monte Carlo (TMCMC) algorithm implemented in the II4U package [52]. The TMCMC algorithm iteratively constructs series of intermediate posterior PDFs

$$\mathbb{P}_j(\theta|\mathcal{D}, M) \propto \mathbb{P}(\mathcal{D}|\theta, M)^{\rho_j} \mathbb{P}(\theta) \quad (9)$$

where $j = 0, \dots, m$ is the index of the Monte Carlo time series (generation index), and $0 < \rho_0 < \rho_1 < \dots < \rho_m = 1$ and ρ_j controls the transition between the generations. The TMCMC method can utilize a large number of parallel chains that are evaluated in each Monte Carlo step to reach a result close to the true posterior PDF.

Since the ratio of model parameters to time-points is small (5:7) for the continuum model, we used all the time-points for the calibration of the continuum model. The validation was performed using the hybrid (discrete-continuum) model using the spatial statistical measures described below.

D. Spatial Analysis - HDC Model Validation

Complete Spatial Randomness Test of Spatial Cell Distributions: The Complete Spatial Randomness (CSR) test examines whether the observed spatial point patterns, in our case the centroids of the nuclei, can be described by a uniform random distribution [53]. The CSR test was performed using Ripley's K -function and the *spatstat* [54] package of R [55]. The K -function [56] is defined as the ratio between the number of the events, i.e. locations of points, j within a distance t from the event i , over the total number of events N , in the studied volume V

$$K(t) = \frac{1}{\hat{\lambda}} \sum_i \sum_{j \neq i} I(d_{ij} < t), \quad I(x) = \begin{cases} 1, & \text{if } x = \text{true} \\ 0, & \text{otherwise} \end{cases} \quad (10)$$

where $\hat{\lambda} = N/V$ denotes the average density of events, N , in the studied volume V , d_{ij} is the distance between events i and j , and t is the search radius. The K -function was calculated across all datasets and compared against complete spatial randomness that follows a Poisson process $K(t) = 4\pi t^3/3$ [56] for three spatial dimensions. Isotropic edge correction was applied in the calculation of the K -function. The volume used for the calculation of the K -function is the same with that used in the simulations, i.e. $2.5 \times 2.5 \times 0.917 \text{ mm}^3$. To assess the uncertainty of the random variable K , we produced a CSR envelope by generating 100 random distributions and calculating the K -function for each of them. The envelope was created by keeping the minimum and maximum values of the resulting K values. A substantial upward separation of the observed K -function from the theoretical random K -function denotes clustered patterns, while a downward separation denotes dispersed patterns [53]. Both separation types suggest non-randomness of the examined spatial distribution.

Characterization of the Spatial Cell Distributions: **Inter-Nucleic Distance Distributions:** The Inter-Nucleic (IN) Distance Distribution for a given sample was calculated by the pairwise Euclidean distances between all nuclei. Given two nuclei i and j with centroid positions $\mathbf{p}_i = (x_i, y_i, z_i)$ and $\mathbf{p}_j = (x_j, y_j, z_j)$ respectively, their pairwise Euclidean distance

is given by $D_{ij} = \sqrt{(x_i - x_j)^2 + (y_i - y_j)^2 + (z_i - z_j)^2}$, $i, j = 1 \dots N$, $i \neq j$ where N the total number of nuclei.

Nearest-Neighbour Distance Distributions: The Nearest-Neighbour (NN) Distance Distribution for a given sample were calculated using the distances between the nearest neighbours of the nuclei. The nearest neighbour distance for a given nucleus i is given by the minimum IN Distance between the nucleus i and all the other nuclei of the sample, i.e. $D_{NN}^i = \min_{i,j} \{D_{ij}\}$, $j \in [1, N]$, $j \neq i$.

The comparisons between the *in-vitro* and *in-silico* IN and NN distance distributions were performed using the cosine similarity test [57], in MATLAB [38] (Supplementary S.4).

III. RESULTS

A. Estimation of the macroscopic model parameters

The continuum Keller-Segel model was used to generate simulation data. The resulting cell density profiles for a given parameter set were compared against the *in-vitro* estimated cell density profiles of a dataset. This process was applied to each of the 12 datasets separately. Approximately 14300 different sets of model parameters were assessed using the TMCMC method for each of the 12 datasets. The obtained manifold of the inferred PDFs for one dataset is presented in Supplementary Fig. S.1a. The marginal distributions and the average values along with their corresponding standard deviations from the posterior PDFs of the model parameters of these datasets are presented in Fig. 5a, and in Supplementary Table S.1. Most of the estimated model parameters exhibited low uncertainty compared to range of their respective prior PDFs. The growth rate s corresponded to a cell doubling time equal to 3.461 ± 0.013 days, (mean \pm SEM). The diffusion constants for the cells, D_u , and chemotactic agents, D_f , suggest that diffusion is more dominant compared to the advection, especially by the end of the simulation (last 3 time-points). This occurs due to the fact that the chemotactic signals diffuse in space, hence their gradient towards the bottom becomes less steep (Supplementary Fig. S.1b). The parameter r was found to have the largest variation and uncertainty across and within the datasets, respectively; hence its contribution may be smaller than the other parameters. To test this, we performed global sensitivity analysis of the model parameters with response to the tumour volume in 3D, and the tumour area at the bottom with density values greater than 10^{-3} . The resulted rank correlation matrix between the model parameters and the outputs confirmed that r contributed less than the rest of the parameters (Supplementary S.2). A visual representation of the *in-silico* produced cell density profiles, presented in Fig. 5b, using the calibrated parameters, shows that the model predictions reproduce the overall behaviour observed in the experiments, i.e. the biased movement of the cells towards the bottom. The Normalized Root Mean Squared Error (NRMSE) of the cell density evaluated at each spatial grid point per time point is presented in Fig. 6, excluding Day 0, when simulation and experimental data were identical.

B. Spatial Analysis & HDC Model Validation

The estimated model parameters were subsequently used in the hybrid model (Fig. 4), separately for each dataset.

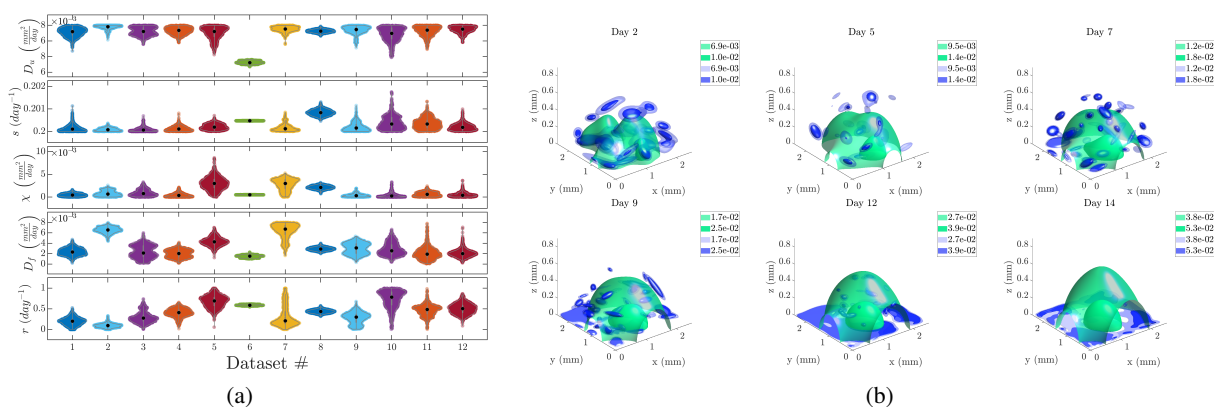


Fig. 5: Inferred model parameters and simulation results (a) Violin plots of the marginalized posterior PDFs of the model parameters across the 12 datasets. The black dots represent the median values. (b) Isosurface plot of the experimental and simulated density results using the inferred parameters of the initial conditions of a representative dataset. The blue colour-map corresponds to the *in-vitro* cell density profiles and the green colour-map corresponds to the *in-silico* cell density profiles.

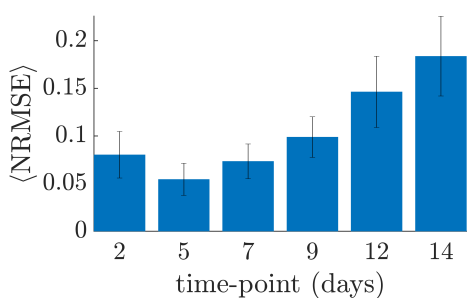


Fig. 6: Average and standard deviation of Normalized Root Mean Squared error across all datasets for 6 time-points.

The resulting *in-silico* cellular coordinates were analysed and compared to the corresponding *in-vitro* coordinates of the centroids from the segmented fluorescent nuclei of the cells. The quantitative characterization of the spatial distributions of the cells was performed using the IN, and NN Euclidean distance distributions. The IN distance distributions quantify the positioning of the cells relative to one another, while the NN distance distributions measure the distances between each cell and their nearest neighbouring cell. The resulting IN distance distributions, depicted in Fig. 7a, show that the distributions remained relatively stable across all samples and time, for both experiments and simulations, with a characteristic peak distance at ~ 1 mm. The cosine similarity test yielded an average similarity value equal to 0.9896 ± 0.0109 , suggesting high similarity between IN distance distributions from experiments and simulations. Their similarity remained high across all time-points, as shown in Fig. 7e (bottom right). On the other hand, the NN distance distributions, presented in Fig. 7b, initially formed, wide distributions that gradually tended to become narrower around lower neighbourhood radii values with respect to time, across all samples, with a characteristic peak at ~ 15 μm for the experiments, and ~ 10 μm for the simulations. These peaks can be interpreted based on the simulations hypotheses, specifically regarding the cell division where the daughter cells are placed next to each other,

and the adhesion that prevents migration. The average cosine similarity between NN distance distributions from experiments and simulations was equal to 0.6184 ± 0.2226 . The similarity between experimental and simulation NN distance distributions decreased as a function of time, as shown in Fig. 7e (bottom right). The different characteristic peaks in the NN Distance Distributions contributed to the decreasing similarity values. We attribute these differences to grid size effects, from which lattice cellular automata typically suffer [20]. An increase of the grid size would correct this error. According to the definition of NN distance, it can be viewed as a special case of the IN distance. In turn, we would expect that the narrowing of the NN distance distributions would destabilize the IN distance distributions. However, the maintenance of their shape can be interpreted as a result of the organization of the cells into smaller clusters that maintained a relatively constant distance, the synchronized division of the cells, as well as their overall accumulation towards the glass bottom of the wells with respect to time.

To investigate the spatial organization of the cells, we performed the CSR test, using Ripley's K -function [56]. Specifically, we examined whether the cells, represented by their nuclei centroids, were randomly distributed in space. The results depicted in Fig. 7c indicate substantial differences from a uniform random distribution for both experiments and simulations. For the experimental data, we observed clustering for a wide range of neighbourhood radii, as well as an increasing dispersion for longer distances across all samples, with respect to time. The results from the simulation data did not exhibit significant differences compared to the results from the experiments until Day 2. Starting on Day 9, we observed that the K -function of the experimental data indicates more pronounced clustering for smaller values of neighbourhood radii, and more pronounced dispersion patterns for longer distances, compared to the K -function of the simulation data.

The spatial distributions of the *in-silico* cells, and the corresponding experimental dataset are presented in Fig. 7d. We observe that both *in-silico* and *in-vitro* cells perform a biased movement towards the bottom, with the *in-silico* cells

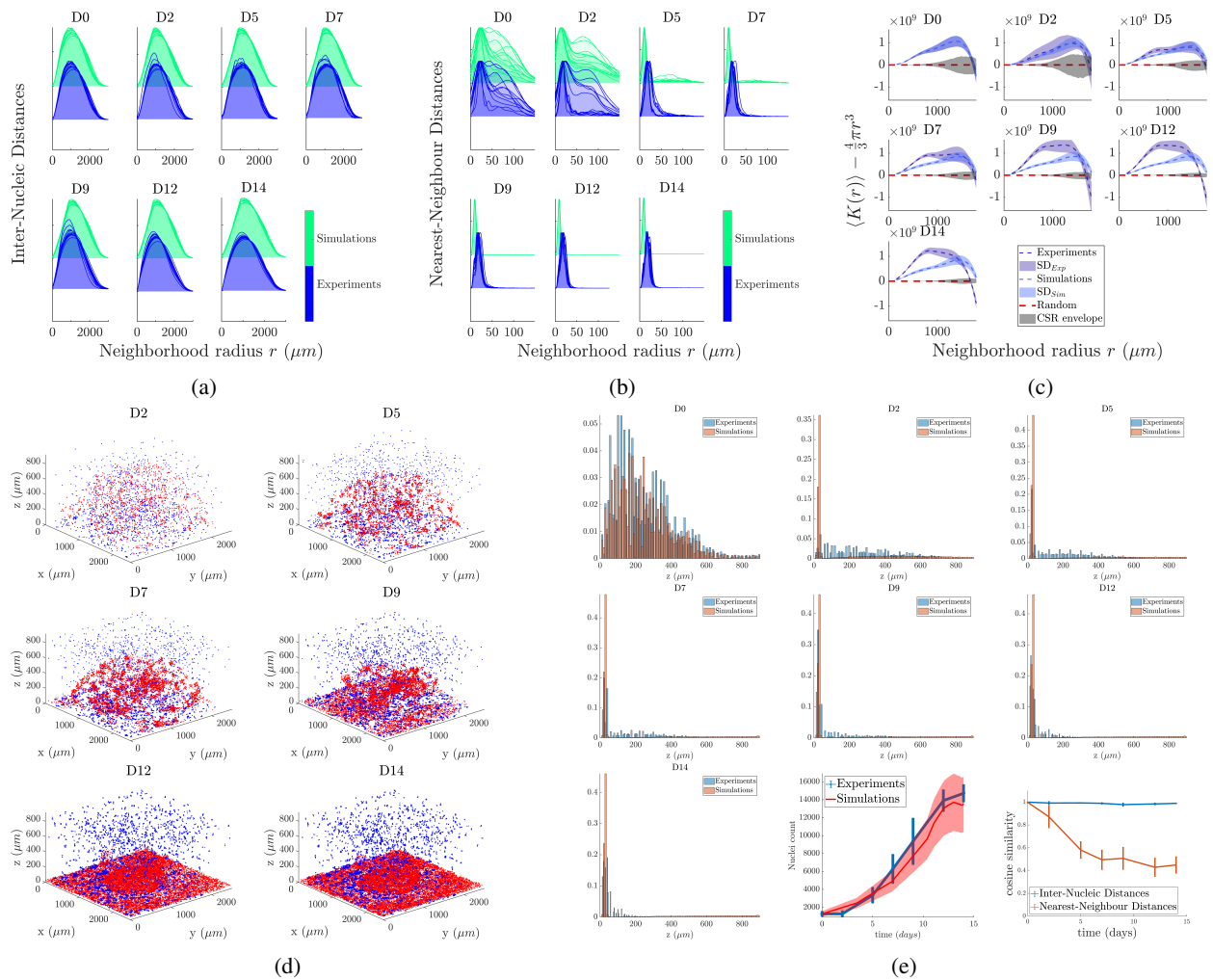


Fig. 7: Spatial analysis and comparisons between experiments and simulations (a) Inter-Nucleic Euclidean distance distributions. The title (D#) denotes the time-point in days. (b) Nearest-Neighbour Euclidean distance distributions. (c) Complete Spatial Randomness test; average values of K -function across all samples and the corresponding standard error of mean (SEM). (d) Spatial distributions of cells from the cellular automaton (blue) and its corresponding experimental dataset (red) with respect to time. (e) Histograms of the number of cells found in the z -dimension. Bottom center: Average number of cells across all datasets with respect to time. The blue bars and the red band represent the standard deviation for the experimental and simulation results, respectively. Bottom right: Cosine similarity test for IN and NN distance distributions between experimental and simulation results.

characterized also by a more pronounced random motion. Similarly, the histograms of the numbers of cells across the z -dimension in Fig. 7e exhibit similarities between experiment and simulations, even though a small amount of cells appears to maintain elevated positions. The *in-vitro* and *in-silico* number of cells with respect to time, shown in Fig. 7e, are in coherence, exhibiting a logistic growth.

IV. DISCUSSION

A. Relation between Morphological patterns and Mechanisms

The continuum KS model consists of diffusion, growth, and advection terms that represent the random motion, proliferation, and biased movement of the cells towards the bottom, respectively. The estimated diffusion constants (Fig. 5a) suggest

that the random motion plays a significant role in the overall cell movement. Together with the unconstrained migration phase, these parameters affect the morphology of cancer by increasing the NN distance values on Day 2 (Fig. 7b). The effect of advection, together with the constrained migration were more apparent after day 2. The two parameters reflect the tendency to form clusters and move the cells towards the bottom. This effect was also observed in the NN distances between days 5 and 14 (Fig. 7b), as well as in the histograms of the number of cells across different z -values (Fig. 7e), which shows a comparable proportion of *in-silico* and *in-vitro* cells near the bottom. The visualization of the cells (Fig. 7d) shows that not all the *in-silico* cells tended to move towards the bottom. This is a result of the fast diffusion of the chemotactic signals, which led to a more uniform distribution

across the z -dimension compared to day 0 (Supplementary Fig. S.1b). The resulting differences in cell attachment to the bottom is also apparent in the K -functions of the experiments and simulations. The *in-vitro* cell accumulation resulted in increased clustering patterns for smaller neighbourhood radii with respect to time. The increase in the adhesion parameter with respect to time restricts migration to the cells that have not reached the bottom, contributing to the resulting NN distances. This parameter contributes also to the increased clustering of the *in-silico* cells shown in Fig. 7c, even though the changes in K -function were very small.

B. Biased movement and cell sedimentation

Despite the fact that chemotactic migration has been studied in both biological and mathematical levels [58], [59], there is very limited discussion on why the cells tend to move towards the bottom in a 3D culture [40]. In this study, we hypothesized that cell sedimentation is a result of active, chemotactic cell migration due to the fact that gravity may not be sufficient to describe this kind of movement. A characteristic example in [40] shows that if cells are cultured on the interface of two hydrogel structures (sandwich model), then they tend to move across the interface and they do not settle on the bottom. Thus, cell sedimentation due to chemotactic migration remains a reasonable hypothesis.

The selected mathematical model was able to reproduce this biased movement, and the overall framework allowed us to quantify the movement in terms of both spatial patterns and underlying mechanisms. The proposed computational part of the framework was able to work in the mesoscopic scale (μm to mm) taking into account between 1000 and 18000 cells in 3D, exhibiting good performance in terms of processing times. The analysis showed that not all of the *in-silico* cells followed the chemotactic gradient. This phenomenon has also been observed by Tweedy et al. [41], but for a different reason. Their study showed that self-generated gradients may favour the leading wave of cells, because they break down chemoattractants; thus, the cells behind the front do not sense a gradient and move randomly. This phenomenon was not visible in our experiments, due to additional factors that contributed to the biased movement of the cells towards the bottom. These include the compression and degradation of Matrigel, as well as vibrations during the transfer of the samples to the microscope. These factors were not considered in the model; however, these differences helped us understand the effect of cell sedimentation in terms of their K -function. Overall, this framework will help us quantify various biological phenomena, such as chemotaxis, and durotaxis.

V. CONCLUSIONS

We presented a novel framework that combines 3D cell culture experiments, multiscale models, parameter estimation, and spatial validation techniques to examine and quantify the morphology and mechanisms of cancer progression. We applied the proposed framework to the case of TNBC cells cultured in Matrigel ECM, and we modeled this behaviour

using a multiscale HDC model. The parameters of the continuum model were estimated using Bayesian inference and a TCMC algorithm. The estimated parameters were used in the HDC model for a more detailed simulation of the spatial distributions of the cells. The results of both experiments and simulations were analysed using spatial statistical analysis techniques to quantify the morphology of both *in-vitro* and *in-silico* cancer progression. The proposed framework enabled us to relate the underlying mechanisms cancer progression with the observed morphological patterns, even though some differences were observed between experiments and simulations, particularly for later time-points. Future improvements may include incorporating a model term for the quantification of the effect of ECM degradation that may be responsible for the introduction of possible biases. The proposed framework can be used to study the growth patterns of heterogeneous cell populations such as cancer cells and fibroblasts, as well as, study cancer progression in the presence of therapy. Importantly, if potential differences in the morphological patterns in the presence and absence of therapy can be identified it would enable us to design therapeutic strategies that control not only the size of tumours, but also their morphological patterns to minimize invasion. Overall, the presented framework yields great promise for a more complete quantitative understanding of the organization and progression of cancer.

REFERENCES

- [1] P. Friedl, J. Locker *et al.*, "Classifying collective cancer cell invasion," *Nature Cell Biology*, vol. 14, no. 8, pp. 777–783, 2012.
- [2] D. S. P. Tan, H. W. W. Potts *et al.*, "The biological and prognostic significance of cell polarity and E-cadherin in grade I infiltrating ductal carcinoma of the breast," *The Journal of Pathology*, vol. 189, no. 1, pp. 20–27, 1999.
- [3] E. T. Roussos, M. Balsamo *et al.*, "Mena invasive (MenaINV) promotes multicellular streaming motility and transendothelial migration in a mouse model of breast cancer," *Journal of Cell Science*, vol. 124, no. 13, pp. 2120–2131, 2011.
- [4] L. Norton, "Conceptual and Practical Implications of Breast Tissue Geometry: Toward a More Effective, Less Toxic Therapy," *The Oncologist*, vol. 10, no. 6, pp. 370–381, 2005.
- [5] A. Kikuchi, S. Kozuma *et al.*, "Fractal tumor growth of ovarian cancer: Sonographic evaluation," *Gynecologic Oncology*, vol. 87, no. 3, pp. 295–302, 2002.
- [6] V. Cristini and J. S. Lowengrub, *Multiscale modeling of cancer: an integrated experimental and mathematical modeling approach*. United Kingdom: Cambridge University Press, 2010.
- [7] A. R. A. Anderson, M. A. J. Chaplain *et al.*, "Single-cell-based models in biology and medicine," *Mathematical Medicine and Biology: A Journal of the IMA*, vol. 25, no. 2, pp. 185–186, 2008.
- [8] H. P. Greenspan, "Models for the Growth of a Solid Tumor by Diffusion," *Studies in Applied Mathematics*, vol. 51, no. 4, pp. 317–340, 1972.
- [9] D. Loessner, J. A. Flegg *et al.*, "Growth of confined cancer spheroids: a combined experimental and mathematical modelling approach," *Integrative Biology*, vol. 5, no. 3, pp. 597–605, 2013.
- [10] A. M. Stein, T. Demuth *et al.*, "A Mathematical Model of Glioblastoma Tumor Spheroid Invasion in a Three-Dimensional In Vitro Experiment," *Biophysical Journal*, vol. 92, no. 1, pp. 356–365, 2007.
- [11] D. J. Warne, R. E. Baker, and M. J. Simpson, "Using Experimental Data and Information Criteria to Guide Model Selection for Reaction-Diffusion Problems in Mathematical Biology," *Bulletin of Mathematical Biology*, vol. 81, no. 6, pp. 1760–1804, jun 2019.
- [12] W. Jin, E. T. Shah *et al.*, "Reproducibility of scratch assays is affected by the initial degree of confluence: Experiments, modelling and model selection," *Journal of Theoretical Biology*, vol. 390, pp. 136–145, 2016.
- [13] B. Tunc, D. Hormuth *et al.*, "Modeling of Glioma Growth with Mass Effect by Longitudinal Magnetic Resonance Imaging," *IEEE Transactions on Biomedical Engineering*, 2021.

- [14] S. Hoehme, F. Bertaux *et al.*, “Model Prediction and Validation of an Order Mechanism Controlling the Spatiotemporal Phenotype of Early Hepatocellular Carcinoma,” *Bulletin of Mathematical Biology*, vol. 80, no. 5, pp. 1134–1171, 2018.
- [15] J. Lipková, P. Angelikopoulos *et al.*, “Personalized Radiotherapy Design for Glioblastoma: Integrating Mathematical Tumor Models, Multimodal Scans, and Bayesian Inference,” *IEEE Transactions on Medical Imaging*, vol. 38, no. 8, pp. 1875–1884, aug 2019.
- [16] D. A. Hormuth, J. A. Weis *et al.*, “A mechanically coupled reaction–diffusion model that incorporates intra-tumoural heterogeneity to predict in vivo glioma growth,” *Journal of The Royal Society Interface*, vol. 14, no. 128, p. 20161010, 2017.
- [17] D. A. I. Hormuth, J. A. Weis *et al.*, “Biophysical Modeling of In Vivo Glioma Response After Whole-Brain Radiation Therapy in a Murine Model of Brain Cancer,” *International journal of radiation oncology, biology, physics*, vol. 100, no. 5, pp. 1270–1279, apr 2018.
- [18] D. Abler, P. Büchler, and R. C. Rockne, “Towards Model-Based Characterization of Biomechanical Tumor Growth Phenotypes,” in *Mathematical and Computational Oncology*, G. Bebis, T. Benos *et al.*, Eds. Cham: Springer International Publishing, 2019, pp. 75–86.
- [19] A. M. Jarrett, D. A. Hormuth *et al.*, “Towards integration of 64Cu-DOTA-trastuzumab PET-CT and MRI with mathematical modeling to predict response to neoadjuvant therapy in HER2 + breast cancer,” *Scientific Reports*, vol. 10, no. 1, p. 20518, 2020.
- [20] K. A. Rejniak and A. R. A. Anderson, “Hybrid models of tumor growth,” *Wiley Interdisciplinary Reviews: Systems Biology and Medicine*, vol. 3, no. 1, pp. 115–125, 2011.
- [21] S. Sanga, H. B. Frieboes *et al.*, “Predictive oncology: A review of multidisciplinary, multiscale in silico modeling linking phenotype, morphology and growth,” *NeuroImage*, vol. 37, pp. S120–S134, 2007.
- [22] L. Tweedy, P. A. Thomason *et al.*, “Seeing around corners: Cells solve mazes and respond at a distance using attractant breakdown,” *Science*, vol. 369, no. 6507, 2020.
- [23] L. Tweedy and R. H. Insall, “Self-Generated Gradients Yield Exceptionally Robust Steering Cues,” *Frontiers in Cell and Developmental Biology*, vol. 8, p. 133, 2020.
- [24] J. Collis, A. J. Connor *et al.*, “Bayesian Calibration, Validation and Uncertainty Quantification for Predictive Modelling of Tumour Growth: A Tutorial,” *Bulletin of Mathematical Biology*, vol. 79, no. 4, pp. 939–974, 2017.
- [25] E. A. B. F. Lima, J. T. Oden *et al.*, “Selection, calibration, and validation of models of tumor growth,” *Mathematical Models and Methods in Applied Sciences*, vol. 26, no. 12, pp. 2341–2368, 2016.
- [26] A. Hawkins-Daarud, S. Prudhomme *et al.*, “Bayesian calibration, validation, and uncertainty quantification of diffuse interface models of tumor growth,” *Journal of Mathematical Biology*, vol. 67, no. 6, pp. 1457–1485, 2013.
- [27] A. Achilleos, C. Loizides *et al.*, “Multi-process dynamic modeling of tumor-specific evolution,” in *13th IEEE International Conference on BioInformatics and BioEngineering*, 2013, pp. 1–4.
- [28] A. Achilleos, C. Loizides *et al.*, “Multiprocess Dynamic Modeling of Tumor Evolution with Bayesian Tumor-Specific Predictions,” *Annals of Biomedical Engineering*, vol. 42, no. 5, pp. 1095–1111, 2014.
- [29] K. Farrell, J. T. Oden, and D. Faghihi, “A Bayesian framework for adaptive selection, calibration, and validation of coarse-grained models of atomistic systems,” *Journal of Computational Physics*, vol. 295, pp. 189–208, 2015.
- [30] E. A. B. F. Lima, D. Faghihi *et al.*, “Bayesian calibration of a stochastic, multiscale agent-based model for predicting in vitro tumor growth,” *bioRxiv*, 2021.
- [31] C. Loizides, D. Iacovides *et al.*, “Model-Based Tumor Growth Dynamics and Therapy Response in a Mouse Model of De Novo Carcinogenesis,” *PLOS ONE*, vol. 10, no. 12, p. e0143840, dec 2015.
- [32] M. M. Jensen, J. T. Jørgensen *et al.*, “Tumor volume in subcutaneous mouse xenografts measured by microCT is more accurate and reproducible than determined by 18 F-FDG-microPET or external caliper,” *BMC Medical Imaging*, vol. 8, no. 1, p. 16, 2008.
- [33] J. A. Hickman, R. Graeser *et al.*, “Three-dimensional models of cancer for pharmacology and cancer cell biology: Capturing tumor complexity in vitro/ex vivo,” *Biotechnology Journal*, vol. 9, no. 9, pp. 1115–1128, 2014.
- [34] N. M. Dimitriou, S. Flores-Torres *et al.*, “Detection and Spatiotemporal analysis of in-vitro 3D migratory Triple-Negative Breast cancer cells,” *bioRxiv*, 2021.
- [35] F. Luisier, C. Vonesch *et al.*, “Fast interscale wavelet denoising of Poisson-corrupted images,” *Signal Processing*, vol. 90, no. 2, pp. 415–427, 2010.
- [36] E. Biot, E. Crowell *et al.*, “A new filter for spot extraction in N-dimensional biological imaging,” in *2008 5th IEEE International Symposium on Biomedical Imaging: From Nano to Macro*. IEEE, 2008, pp. 975–978.
- [37] S. R. Sternberg, “Biomedical image processing,” *Computer*, no. 1, pp. 22–34, 1983.
- [38] MATLAB, *9.7.0.1190202 (R2019b)*. Natick, Massachusetts: The MathWorks Inc., 2018.
- [39] Z. I. Botev, J. F. Grotowski *et al.*, “Kernel density estimation via diffusion,” *The annals of Statistics*, vol. 38, no. 5, pp. 2916–2957, 2010.
- [40] H. Liu, T. Lu *et al.*, “A microcarrier-based spheroid 3D invasion assay to monitor dynamic cell movement in extracellular matrix,” *Biological Procedures Online*, vol. 22, no. 1, p. 3, 2020.
- [41] L. Tweedy, D. A. Knecht *et al.*, “Self-Generated Chemoattractant Gradients: Attractant Depletion Extends the Range and Robustness of Chemotaxis,” *PLOS Biology*, vol. 14, no. 3, p. e1002404, mar 2016.
- [42] O. Susanto, Y. W. H. Koh *et al.*, “LPP3 mediates self-generation of chemotactic LPA gradients by melanoma cells,” *Journal of Cell Science*, vol. 130, no. 20, pp. 3455–3466, 2017.
- [43] T. Hillen and K. Painter, “Global Existence for a Parabolic Chemotaxis Model with Prevention of Overcrowding,” *Advances in Applied Mathematics*, vol. 26, no. 4, pp. 280–301, 2001.
- [44] J. Douglas and J. E. Gunn, “A general formulation of alternating direction methods,” *Numerische Mathematik*, vol. 6, no. 1, pp. 428–453, 1964.
- [45] P. Lax and B. Wendroff, “Systems of conservation laws,” *Communications on Pure and Applied Mathematics*, vol. 13, no. 2, pp. 217–237, 1960.
- [46] B. van Leer, “Towards the ultimate conservative difference scheme. V. A second-order sequel to Godunov’s method,” *Journal of Computational Physics*, vol. 32, no. 1, pp. 101–136, 1979.
- [47] G. Strang, “On the construction and comparison of difference schemes,” *SIAM journal on numerical analysis*, vol. 5, no. 3, pp. 506–517, 1968.
- [48] A. R. A. Anderson, *A Hybrid Discrete-continuum Technique for Individual-based Migration Models*. Basel: Birkhäuser Basel, 2003, pp. 251–259.
- [49] A. R. A. Anderson, “A hybrid mathematical model of solid tumour invasion: the importance of cell adhesion,” *Mathematical Medicine and Biology: A Journal of the IMA*, vol. 22, no. 2, pp. 163–186, 2005.
- [50] L. C. Franssen, T. Lorenzi *et al.*, “A Mathematical Framework for Modelling the Metastatic Spread of Cancer,” *Bulletin of Mathematical Biology*, vol. 81, no. 6, pp. 1965–2010, 2019.
- [51] N. P. A. D. Gunasinghe, A. Wells *et al.*, “Mesenchymal–epithelial transition (MET) as a mechanism for metastatic colonisation in breast cancer,” *Cancer and Metastasis Reviews*, vol. 31, no. 3, pp. 469–478, 2012.
- [52] P. E. Hadjidoukas, P. Angelikopoulos *et al.*, “II4U: A high performance computing framework for Bayesian uncertainty quantification of complex models,” *Journal of Computational Physics*, vol. 284, pp. 1–21, 2015.
- [53] W. de Back, T. Zerjatke, and I. Roeder, *Statistical and Mathematical Modeling of Spatiotemporal Dynamics of Stem Cells*. New York, NY: Springer New York, 2019, pp. 219–243.
- [54] A. J. Baddeley, R. Turner, and Others, “Spatstat: An R package for analyzing spatial point patterns,” 2004.
- [55] R Core Team, “R: A Language and Environment for Statistical Computing,” Vienna, Austria, 2020. [Online]. Available: <https://www.r-project.org/>
- [56] P. M. Dixon, “Ripley’s K Function,” *Wiley StatsRef: Statistics Reference Online*, vol. 3, pp. 1796–1803, 2014.
- [57] J. Han, M. Kamber, and J. Pei, “2 - Getting to Know Your Data,” in *The Morgan Kaufmann Series in Data Management Systems*, J. Han, M. Kamber, and J. B. T. D. M. T. E. Pei, Eds. Boston: Morgan Kaufmann, 2012, pp. 39–82.
- [58] E. T. Roussos, J. S. Condeelis, and A. Patsialou, “Chemotaxis in cancer,” *Nature Reviews Cancer*, vol. 11, no. 8, pp. 573–587, 2011.
- [59] F. Bubba, C. Pouchol *et al.*, “A chemotaxis-based explanation of spheroid formation in 3D cultures of breast cancer cells,” *Journal of Theoretical Biology*, vol. 479, pp. 73–80, 2019.